Iraqi Geological Journal

Journal homepage: https://www.igj-iraq.org

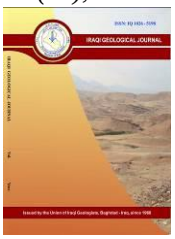

U-Hf-Pb Isotope Zircon Data on A Basaltic Dyke in the Pushtashan Ophiolite, NE Iraq: Implication for Tectonic Switching of the Neo-Tethyan

Heider S. Al Humadi[1,2*], Jaakko Kara[2], Markku Väisänen[2], Sabah A. Ismail[3], Hugh O'Brien[4], Yann Lahaye[4], and Esa Heilimo[2]

[1] Department of Applied Geology, College of Science, University of Babylon, Iraq
[2] Department of Geography and Geology, University of Turku, Finland
[3] Department of Applied Geology, College of Sciences, Kirkuk University, Kirkuk, Iraq
[4] Geological Survey of Finland, Espoo, Finland
* Correspondence: sci.heider.humadi@uo.babylon.edu.iq

Received:
21 August 2025
Accepted:
3 January 2026
Published:
31 March 2026

Abstract

Magmatic activity of varying ages along the Zagros Orogenic Belt reflects the transition from the Neo-Tethyan oceanic subduction to continental collision. Within the Pushtashan ophiolite of northeastern Iraq, two compositionally and temporally distinct basaltic units have been identified: older and younger basalts. The younger basalt occurs as dyke, that intrude the older basalts and are notably different from the older units in both age and tectonic setting. We present here new zircon U-Pb radiometric data with Hf isotopic data for the younger basalt. The U–Pb results yield a crystallization age of 74 ± 1 Ma. Initial ε_{Hf} values show a range from -1 to +10, with an average of +5, indicating a magma source of juvenile mantle material with notable assimilation of older continental crust. When integrated with published U–Pb ages from other magmatic rocks across the Zagros Orogenic Belt, our results constrain a series of younger magmatic pulses formed during alternating extensional and compressional phases of the accretionary orogen. We propose that the 74 Ma Pushtashan basaltic dyke, along with coeval magmatic events in the Zagros Orogenic Belt, record tectonic switching between advancing and retreating subduction processes, which governed the alternating geodynamic regimes along the Neo-Tethyan margin.

Keywords: Extensional setting; Geochronology; Hf isotope; Pushtashan ophiolite

1. Introduction

Ophiolites are fragments of oceanic crust and upper mantle preserved in orogenic belts (Coleman, 1977). They develop at divergent plate environments and are emplaced at convergent plate boundaries (Furnes and Dilek 2017). The association of rock assemblages in ophiolites from ultramafic to felsic (Furnes et al., 2020) has been used as a tool to understand the ophiolite formation processes within mid-oceanic ridges, subduction zones, back-arc basins and continental growth mechanisms during plate collisions (Dilek and Robinson, 2003). Ophiolites are broadly divided into subduction-related and subduction-unrelated types based on various combinations of immobile elements (Pearce, 2014; Furnes and Dilek, 2017; Furnes et al., 2020). However, besides the general classifications, it is important to date the tectono-magmatic events related to ophiolites for a better understanding of the processes involved in their formation, emplacement, later magmatism and broader tectonic evolution.

The Zagros Orogenic Belt (ZOB) represents an example of an area hosting numerous ophiolites (Fig. 1). The initial collision of the Arabian and Eurasian plates started in the Tertiary (Agard et al.,

2011), resulting in the closure of the Neo-Tethyan Ocean in the Late Cretaceous and the formation of ZOB, which is interpreted as an accretionary complex (Agard et al., 2011; Ghasemi and Talbot, 2006). The ophiolites along the ZOB are disconnected allochthons and define the boundary between the Arabian and Eurasian plates. The ophiolites of Iraq were emplaced in the Mesozoic and Cenozoic ages. Mesozoic ones include the Mawat, Penjwen, Bulfat, Pushtashan, and Hasanbag ophiolites (Ali et al., 2012; Mohammad et al., 2017; Al Humadi et al., 2019; Ismail et al., 2017, 2020), wheras the Cenozoic ophiolitic assemblages are smaller and less well-preserved and occur as mélange-like incomplete fragments within the Walash-Naopurdan Group, including the Rayat and Qandil complexes (Arai et al., 2006).

The Pushtashan ophiolite (PO) is a part of the Neo-Tethyan oceanic crust exposed in the Iraqi Zagros Suture Zone (IZSZ), about 130 km north of Sulaimani city, NE Iraq (Fig. 2). Many of these above-mentioned ophiolites preserve post-emplacement magmatic events whose tectonic setting and geodynamic implications remain poorly understood. In this study, we report single-grain laser-ablation U–Pb zircon ages and zircon Hf isotopic data of a basaltic dyke from the crustal section of the PO. These results allow us to assess the age and source characteristics of the dyke and to discuss their implications for the tectono-magmatic evolution of the PO and other ophiolites across the Zagros Orogenic Belt.

2. Geological Background

2.1. Geology of the Iraqi Zagros Suture Zone

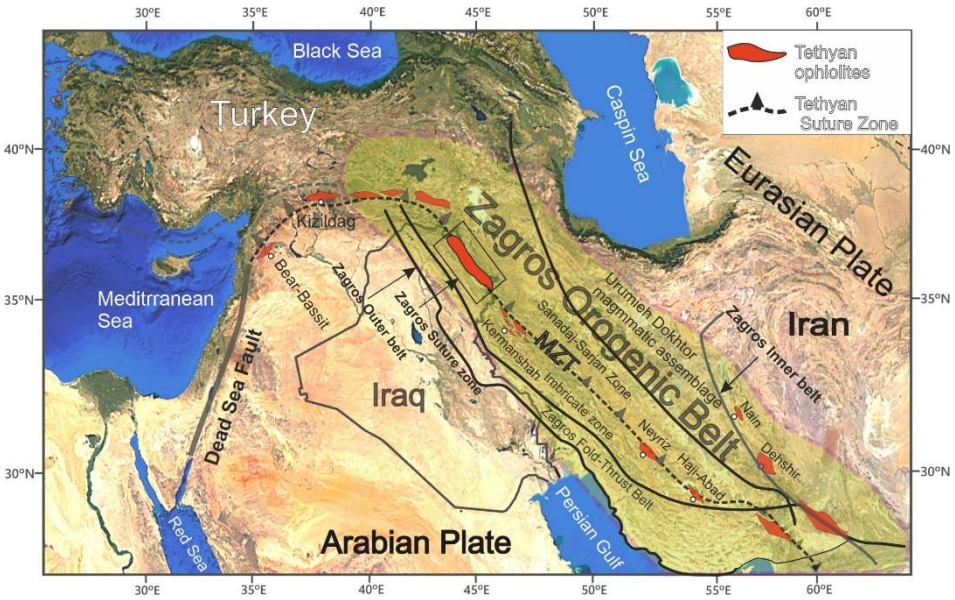

Fig. 1. Distribution of Tethyan ophiolites in the Zagros Orogenic Belt (modified from Dilek et al., 2003). Tectonic units are modified from Alavi (1994). The locations of ophiolites, the Outer and Inner Zagros belts, and the Main Zagros Thrust (MZT) are indicated

The ZOB represents the middle section of the Alpine-Himalayan Belt (Fig. 1), which extends for 10000 km from northwestern Africa in the west, through the European Alps, the Balkan Peninsula, the eastern Mediterranean region, in Zagros (Iraq-Iran) and Oman, in the west Indian Ocean to the Tibetan-Himalaya in the east and Indochina Peninsula in the southeast (Furnes et al., 2020). The ZOB consists of four parallel tectonic units, arranged from northeast to southwest: the Urumieh–Dokhtar magmatic arc, the Sanandaj–Sirjan unit, the imbricate unit and the Zagros fold-thrust belt (Alavi,

1994). The fold-thrust belt and the Sanandaj-Sirjan unit are also known as the inner and outer Zagros belts, respectively, which are divided by the Main Zagros Thrust (MZT) (Moghadam and Stern, 2011).

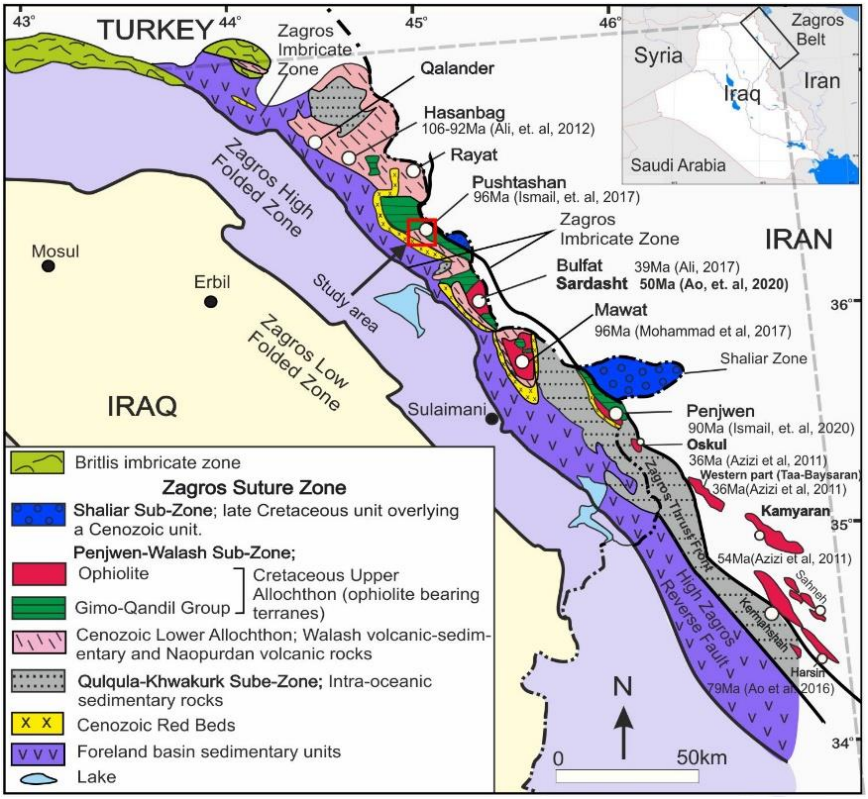

Fig 2. Regional tectonic map of the Kurdistan region, NE Iraq, showing the major tectonic subdivisions modified from Fouad (2015)

Subdivision of the Zagros inner and outer belts (Moghadam and Stern, 2011) considers the ophiolites along the IZSZ as part of the Zagros outer belt. Aswad (2016) suggested that the IZSZ comprises two allochthonous blocks, the upper and lower blocks formed during the Neo-Tethyan ocean subduction. The obduction of the oceanic lithosphere onto the Arabian Plate occurred during the late Cretaceous and Neogene ages (Jassim and Goff, 2006). Tectonically, three units are recognised within the IZSZ: the Qulqula-Khwakurk, Panjwen-Walash, and Shalair units (Fig. 2) (Budy and Jassim, 1987; Jassim and Goff, 2006). The Qulqula-Khwakurk unit comprises limestone and radiolarian chert. The Penjwen-Walash unit consists of two distinct thrust sheets: the upper allochthon is the Cretaceous Gimo-Qandil group, the lower one is the Cenozoic Naupordan-Walash group (Aswad et al., 2016). The upper allochthon is the ophiolite-bearing terrane. The Shalir unit is part of the Sanandaj-Sirjan domain and comprises a metamorphic basement of pre-Cretaceous ages (Sengör, 1984) (Fig. 2).

2.2. Geology of the Pushtashan ophiolite

The PO is the remnant of the Neo-Tethys oceanic crust exposed within the IZSZ in northeastern Iraq (Kurdistan region), consisting of volcanic rocks intruded by plutonic rocks. The volcanic rocks make up the upper part of the PO comprising pillowed basalts and andesites, and are overlain by sedimentary rocks. Quartz veins occur within the basaltic and andesitic rocks (Ismail et al., 2017) (Fig. 3). Tectonic contacts separate the PO assemblages, and a thrust fault occurs between the volcanic rocks and the Cretaceous Qandil Group. Plutonic rocks represent the middle part of the ophiolite and

are composed of norites and gabbros with associated felsic dykes as well as a mantle section of serpentinized peridotites.

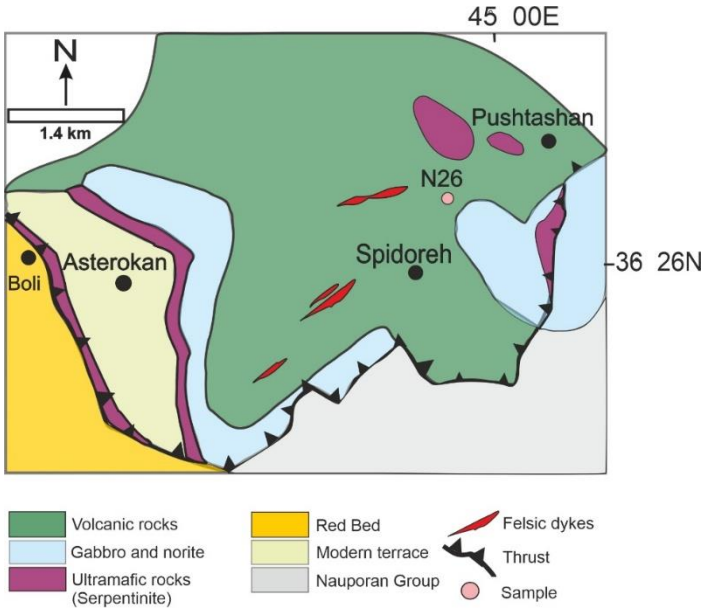

Fig. 3. Geological map of the Pushtashan ophiolite modified after (Ismail et al., 2017)

The felsic rocks are granodiorites and trondhjemites, granodiorites have been dated to 96 ± 2 Ma (Ismail et al., 2017). The gabbros and norites intrude the volcanic rock as sills (Buday and Jassim, 1987). A pegmatitic gabbro dyke is also present, and felsic intrusions occur in the upper and lower parts of the ophiolite (Ismail et al., 2017). Partly serpentinized peridotites occur in the lower part of the ophiolite.

3. The Sample and Research Methods

A basaltic dyke is exposed within PO and located at coordinates of (N 36º.439', E 45º.001'), dark grey in color, fine-grained to aphanitic texture in hand specimen. The dyke intrudes volcanic basalts and andesites as an irregular, fragmented, consisting of plagioclase and pyroxene, and accessory minerals like ilmenite, chlorite, and magnetite. Fine-grained plagioclase is a common mineral showing sub-ophitic texture, weak lamellae and is partly altered to sericite and calcite (Fig. 4). The dyke was selected for zircon U-Pb and Lu-Hf analysis, and sample N26 was previously analysed for geochemistry by Ismail et al. (2017). The zirconium content is 298 ppm, and the dyke is geochemically classified as alkali basalt (Ismail et al., 2017).

3.1. U-Pb Geochronology of Zircon

The zircon separation process was carried out at the University of Turku, following a sequence of crushing and grinding, panning, heavy liquid separation, magnetic separation, and finally, hand-picking.

The grains were mounted on double-sided tape, glued with epoxy, and polished. The specific spots selected for analysis were based on Back Scattered Electron (BSE) images. This was performed using a JEOL JSM-7100F FE-SEM Schottky, equipped with an Oxford Instruments energy dispersive spectrometer (EDS) X-max (80 mm2). These procedures were conducted at the Finnish Geosciences Research Laboratory within the Geological Survey of Finland in Espoo.

The U-Pb zircon dating was carried out using a Nu AttoM single collector ICP-MS at the Geological Survey of Finland, Espoo, following a similar approach to that described by Kara et al. (2018).

Ablation conditions were: beam diameter: 25µm, pulse frequency: 5Hz, beam energy density: 2J/cm^2. A single U-Pb measurement included a short pre-ablation, 15s of on-mass background measurement, followed by 30s of ablation with a stationary beam. Zircon standards GJ-1 (609 ± 1 Ma; Belousova et al., 2006), Plešovice (PL; 337 ± 0.4 Ma; Sláma et al., 2007), and the in-house standard A382 (1877 ± 2 Ma; Huhma et al., 2012) were analyzed at the beginning and end of each session, and periodically throughout. Raw data were corrected for background, laser-induced fractionation, mass discrimination, and ion counter drift, and calibrated against concordant reference zircons using GLITTER (Van Achterbergh et al., 2001).

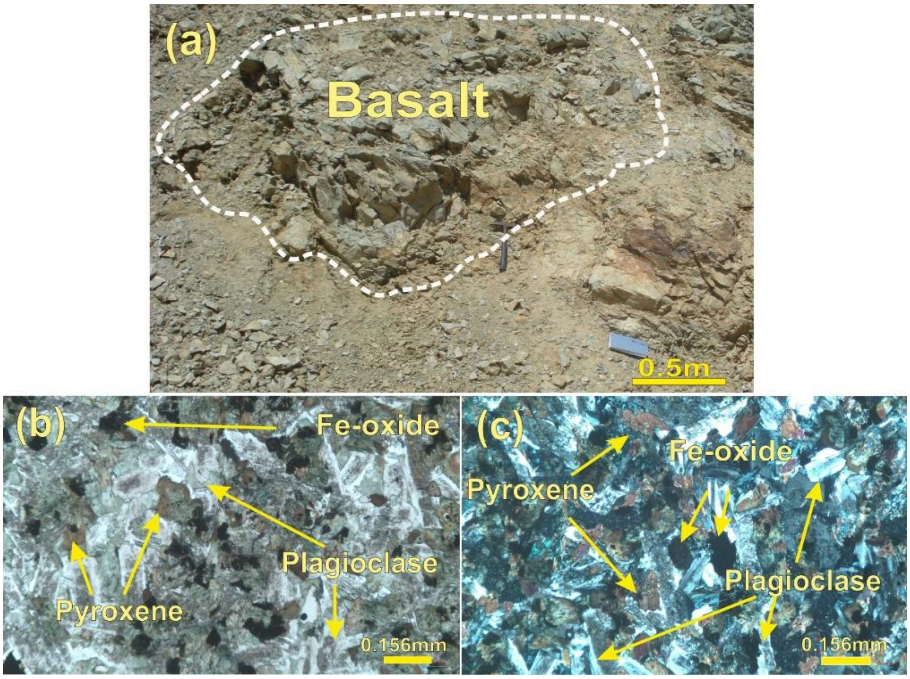

Fig. 4. a) Field photograph from the PO, showing the basaltic rock. b and c) Photomicrograph of the basaltic rock, of PPL and XPL, aphanitic texture of fine-grained pyroxene, plagioclase and Iron oxides

Subsequent data reduction, including common Pb correction and error propagation, was performed with an in-house Excel sheet. Reported uncertainties include within-run analytical errors (SD) combined with standard reproducibility (SE). To reduce elemental fractionation, the ablation pit depth-to-diameter ratio was minimized, and homogeneous time segments were matched to corresponding intervals in the reference zircon. Final U–Pb data plots and age calculations were generated using Isoplot/Ex 4.15 (Ludwig, 2003).

3.2. Hf Isotope Analysis of Zircon

Lu–Hf isotope analyses were carried out at the Geological Survey of Finland, Espoo, using a Nu Plasma HR multicollector ICP-MS, following procedures similar to those described by Heinonen et al. (2010), with the exception that a Photon Machine Analyte G2 laser microprobe was employed. Sample ablation was performed in He gas (flow rates of 0.4 and 0.1 L/min) within a HelEx ablation cell (Müller et al., 2009). All analyses were conducted in static ablation mode with a beam diameter of 50 µm, a pulse frequency of 5 Hz, and an energy density of 2.8 J/cm².

Before each ablation, a 30-second on-mass background measurement was recorded. The MC-ICP-MS was fitted with nine Faraday detectors and amplifiers equipped with 10^{11} Ω resistors. During ablation, data were collected in static mode for isotopes ^{173}Yb, ^{175}Lu, ^{176}Hf–Yb–Lu, ^{177}Hf, ^{178}Hf, and ^{179}Hf. For zircons with typical Hf concentrations, total Hf signal intensities ranged from 1.0 to 2.0 V.

Isotopic data were acquired using Nu Plasma time-resolved analysis software, and final isotopic ratios were calculated offline using an in-house Excel spreadsheet.

The raw data were filtered at 2s and corrected for mass discrimination using the exponential law. The mass discrimination factor for Hf was determined assuming $^{179}Hf/^{177}Hf=0.7325$ (Patchett and Tatsumoto, 1981). The Yb interference correction is crucial for precise and accurate $^{176}Hf/^{177}Hf$ obtained by laser ablation analysis (e.g., Kemp et al., 2009a, 2009b). In the present study, the effect of the Yb correction has been evaluated on an in-house standard (LV11, Heinonen et al, 2010) with Yb/Hf ratios similar to many of the studied zircons. A range of Yb isotope ratios is reported in the literature (e.g., Vervoort et al., 2004), and we have used the $^{176}Yb/^{173}Yb$ value of 0.7961 from Chu et al (2002) for the correction of the ^{176}Yb interference on ^{176}Hf. The $^{176}Lu/^{175}Lu$ value of 0.02656 has also been used for the correction of the ^{176}Lu interference on ^{176}Hf (Scherer et al, 2001; Vervoort et al, 2004).

A value for the decay constant of ^{176}Lu of 1.867×10^{-11} a^{-1} has been used in all calculations (Söderlund et al., 2004; Scherer et al., 2001). For the calculation of ε_{Hf} values, we use present-day chondritic $^{176}Hf/^{177}Hf=0.282785$ and $^{176}Lu/^{177}Hf=0.0336$ (Bouvier et al., 2008). The reference zircon GJ-1 was run as an unknown at frequent intervals. Multiple LA-MC-ICP-MS analyses, using the same instrumental parameters, of the reference zircon GJ-1 during the course of the present study yielded a $^{176}Hf/^{177}Hf$ of 0.28194±10 (2s, n=35, which is within error to results obtained by solution MC-ICP-MS analyses for GJ1 (0.281998±7, Gerdes and Zeh 2006; 0.282000±5, Morel et al., 2008). The average $^{176}Hf/^{177}Hf$ value of LV11 was 0.28274±11 (2s, n=39, which is within error with the results obtained by solution MC-ICP-MS analyses by Heinonen et al. (2010): 0.28283 ± 3.

4. Results

4.1. U-Pb Data

The zircons are typically subhedral or broken grains, but euhedral grains also exist. The grains are 50–170μm in length and 20–100μm in width. A few grains occasionally show internal zoning. Black spots of plagioclase and white spots of unidentified Th-U-rich phase mineral inclusions are observed in the BSE-images (Fig. 5). In all, 37 spots on 34 grains were analysed. The largest population consists of 24 analyses, which yields a concordia age of 73.77 ± 0.61 Ma (2σ, MSWD = 0.036; Fig. 6a, b and c) and an almost identical weighted average 206Pb/238U age of 73.80 ± 0.61 Ma (2σ, MSWD = 1.19). These are hereafter referred to as 74 ± 1 Ma. Six analyses (purple colour) plot on the concordia curve and form a continuous decreasing range of 206Pb/238U ages from 70 to 48Ma (Fig. 6a; Table 1). Seven analyses (red colour) were omitted from the age calculations due to high discordancy (Fig. 6a).

4.2. Hf isotope Analysis

Seventeen analyses of Hf were conducted on seventeen zircon grains (Table 2). Calculating the initial εHf values, the 74 Ma age was used. The analysis showed initial $^{176}Hf/^{177}Hf$ values between 0.28270 and 0.28303, corresponding to initial εHf values between -1.2 and +10.1 with an average value of +5.1 (Fig. 7). The zircons show $^{176}Lu/^{177}Hf$ values between 0.001 and 0.007 and $^{176}Yb/^{177}Hf$ values between 0.025 and 0.239.

5. Discussion

5.1. Age and Source of the ZOB Magmatism

Twenty-four analyses yield a concordia age of 74 ± 1 Ma, verified by the almost identical weighted average $^{206}Pb/^{238}U$ age. This is interpreted to be the crystallization age of the basaltic dyke.

The interpretation is supported by the sub- to euhedral zircon morphology, growth zoning and high Th/U ratios of the zircons (average 1.51) (Table 2), suggesting that the zircons have a magmatic origin (Kirkland et al., 2015). Moreover, the BSE-images display that the zircons are characterized by black spots of plagioclase, unidentified minerals and bright spots of Th- U- rich phases (Fig. 5) similar to those of the magmatic zircons in the gabbro from the Mawat ophiolite (Al Humadi et al., 2019).

Table 1. U–Pb zircon data for basaltic sample

Sample	Concentrations (ppm)			Ratios		Ages															
	Pb	Th	U	Th/U	Pb206/Pb204	207Pb/206Pb	1s	207Pb/235U	1s	206Pb/238U	1s	r	% Concordance	207Pb/206Pb	1s	207Pb/235U	1s	206Pb/238U	1s
N26-22	3	233	347	0.67	10241	0.04615	0.00125	0.04764	0.00159	0.00749	0.00016	0.5798	61	5	64	47	2	48	1
N26-8	4	392	264	1.49	9898	0.04614	0.00123	0.06019	0.00198	0.00946	0.00020	0.5864	75	5	63	59	2	61	1
N26-19	12	1427	773	1.84	29314	0.04791	0.00062	0.06364	0.00150	0.00963	0.00020	0.8362	52	95	30	63	1	62	1
N26-9	6	442	377	1.17	16004	0.04678	0.00088	0.06919	0.00187	0.01073	0.00022	0.7203	82	38	44	68	2	69	1
N26-7	8	788	510	1.55	21819	0.04825	0.00074	0.07185	0.00179	0.01080	0.00022	0.7867	48	111	36	70	2	69	1
N26-6	8	180	651	0.28	27547	0.04609	0.00082	0.06904	0.00183	0.01086	0.00022	0.7375	230	3	43	68	2	70	1
N26-3	5	424	297	1.42	13061	0.04713	0.00101	0.07190	0.00209	0.01106	0.00023	0.6756	63	56	50	71	2	71	1
N26-10	9	965	531	1.82	23373	0.04779	0.00071	0.07348	0.00181	0.01115	0.00023	0.8005	60	89	35	72	2	71	1
N26-35	4	352	271	1.30	11756	0.04852	0.00107	0.07474	0.00219	0.01117	0.00023	0.6618	39	125	51	73	2	72	1
N26-14a	7	739	408	1.81	18009	0.04563	0.00080	0.07039	0.00185	0.01119	0.00023	0.7452	341	-22	42	69	2	72	1
N26-25	5	166	377	0.44	16627	0.04630	0.00083	0.07212	0.00191	0.01130	0.00023	0.7386	123	13	42	71	2	72	1
N26-34	10	992	560	1.77	24817	0.04897	0.00070	0.07684	0.00186	0.01138	0.00023	0.8092	42	146	33	75	2	73	1
N26-16	7	756	422	1.79	18965	0.04795	0.00078	0.07530	0.00193	0.01139	0.00023	0.7707	54	97	38	74	2	73	1
N26-23	8	618	539	1.15	24003	0.04631	0.00068	0.07274	0.00178	0.01139	0.00023	0.8031	160	14	35	71	2	73	1
N26-11	11	1056	632	1.67	28459	0.04715	0.00063	0.07407	0.00176	0.01139	0.00023	0.8279	88	57	32	73	2	73	1
N26-21b	7	646	405	1.59	18156	0.04881	0.00082	0.07698	0.00198	0.01144	0.00023	0.7577	41	139	39	75	2	73	1
N26-32	10	1047	562	1.86	25041	0.04685	0.00069	0.07397	0.00182	0.01145	0.00023	0.8032	103	42	35	72	2	73	1
N26-14b	8	730	453	1.61	20510	0.04770	0.00075	0.07550	0.00191	0.01148	0.00023	0.7803	61	84	37	74	2	74	1
N26-1	6	473	332	1.42	15192	0.04619	0.00090	0.07321	0.00203	0.01150	0.00024	0.7068	129	7	46	72	2	74	2
N26-43	7	654	398	1.64	17840	0.04724	0.00085	0.07555	0.00201	0.01160	0.00024	0.7379	72	62	42	74	2	74	2
N26-36	7	688	424	1.62	19055	0.04838	0.00080	0.07737	0.00198	0.01160	0.00024	0.7631	48	118	39	76	2	74	2
N26-26	9	847	507	1.67	23024	0.04808	0.00072	0.07710	0.00190	0.01163	0.00024	0.7980	56	103	35	75	2	75	2
N26-2	4	297	285	1.04	13244	0.04768	0.00098	0.07681	0.00218	0.01168	0.00024	0.6885	54	83	48	75	2	75	2
N26-46	6	571	350	1.63	15809	0.04879	0.00090	0.07861	0.00211	0.01169	0.00024	0.7300	41	138	43	77	2	75	2
N26-41	7	610	414	1.47	18751	0.04672	0.00081	0.07556	0.00198	0.01173	0.00024	0.7498	100	35	41	74	2	75	2
N26-47b	5	418	310	1.35	14004	0.04804	0.00100	0.07772	0.00222	0.01173	0.00024	0.6838	49	101	49	76	2	75	2
N26-17	6	490	339	1.45	15822	0.04755	0.00088	0.07766	0.00209	0.01185	0.00024	0.7274	62	77	43	76	2	76	2
N26-45	11	1074	569	1.89	26052	0.04664	0.00069	0.07628	0.00187	0.01186	0.00024	0.8007	127	31	35	75	2	76	2
N26-40	10	957	537	1.78	24713	0.04895	0.00071	0.08033	0.00196	0.01190	0.00024	0.8056	44	146	34	78	2	76	2
N26-39	3	206	193	1.06	9014	0.04823	0.00125	0.08016	0.00259	0.01206	0.00025	0.5960	41	110	60	78	2	77	2
N26-29	8	973	659	1.48	21403	0.05859	0.00084	0.06732	0.00164	0.00833	0.00017	0.8094	9	552	31	66	2	53	1
N26-4	9	858	612	1.40	23115	0.05996	0.00077	0.07840	0.00184	0.00948	0.00019	0.8383	10	602	28	77	2	61	1
N26-18	5	330	419	0.79	16343	0.05411	0.00094	0.07407	0.00193	0.00993	0.00020	0.7467	15	375	39	73	2	64	1
N26-21a	8	748	459	1.63	20571	0.05144	0.00078	0.08120	0.00202	0.01145	0.00023	0.7893	25	260	35	79	2	73	1
N26-30	5	348	271	1.29	12503	0.05648	0.00119	0.09060	0.00259	0.01163	0.00024	0.6774	14	471	46	88	2	75	2
N26-20	12	1130	609	1.86	28569	0.06850	0.00075	0.11270	0.00255	0.01193	0.00024	0.8733	9	884	23	108	2	76	2
N26-47a	5	407	312	1.30	14297	0.06498	0.00112	0.10640	0.00276	0.01188	0.00024	0.7495	9	774	36	103	3	76	2

The zircon Lu-Hf analysis can be used to define the basaltic magma origin source, using the $^{176}Hf/^{177}Hf$ ratios to calculate the initial ε_{Hf} value, which is a responsive indicator of whether the magma origin forms from an older (negative ε_{Hf} value) or juvenile (positive ε_{Hf} value) source (e.g., Kinny and Maas, 2003).

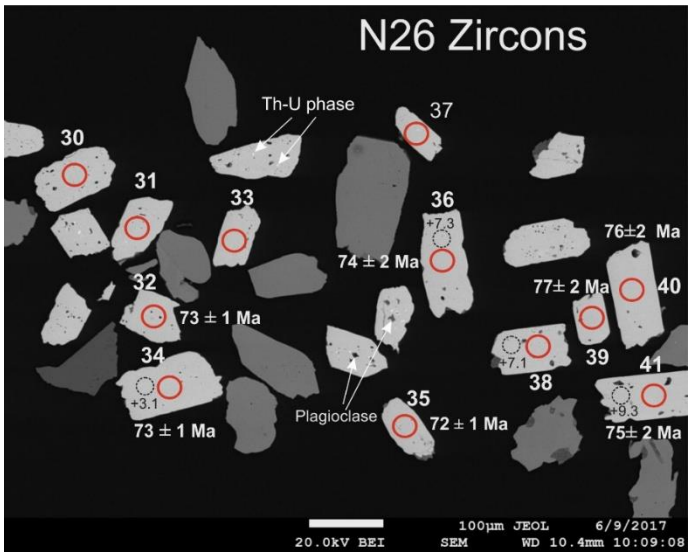

Fig. 5. Back Scattered Electron image of selected zircons. Dark inclusions are plagioclase and the bright ones are unidentified Th-U mineral. Red solid circles are U-Pb spots (25µm) with $^{206}Pb/^{238}U$ age. Black dashed circles are the Lu-Hf spots (50µm) with initial $\varepsilon_{Hf\ (t)}$ values

Zircon grains retain the original $^{176}Hf/^{177}Hf$ ratios due to their very low Lu/Hf ratios, offering a complete record of the Hf isotope compositions of parent magmas during zircon crystallization (e.g., Vervoort and Kemp, 2009). The zircons from the studied sample show a positive average initial ε_{Hf} value of + 5.1 at 74 Ma, with the highest value of +10.1 and the lowest value of -1.2 (Table 2; Fig. 6).

Table 2. Table of the zircon Lu–Hf isotope analytical data for the basalt sample.

Sample	176Hf/177Hf	2s	178Hf/177Hf	2s	176Lu/177Hf	2s	176Yb/177Hf	2s	176Hf/177Hf i	2s	eHf*	2s	Time (Ga)
N26-29	0.282726	0.000054	1.467117	0.000052	0.00384	0.00008	0.1002	0.0023	0.282721	0.000054	-0.6	1.9	0.074
N26-34	0.282833	0.000047	1.467185	0.000029	0.00564	0.00018	0.1594	0.0055	0.282825	0.000047	3.1	1.7	0.074
N26-36	0.282953	0.000029	1.467135	0.000027	0.00437	0.00005	0.1218	0.0014	0.282947	0.000029	7.4	1.0	0.074
N26-38	0.282941	0.000027	1.467178	0.000026	0.00114	0.00002	0.0250	0.0004	0.282939	0.000027	7.1	1.0	0.074
N26-43	0.283011	0.000042	1.467213	0.000033	0.00419	0.00019	0.1223	0.0058	0.283005	0.000042	9.4	1.5	0.074
N26-41	0.283010	0.000028	1.467174	0.000029	0.00703	0.00007	0.1954	0.0019	0.283000	0.000028	9.3	1.0	0.074
N26-45	0.282915	0.000038	1.467186	0.000033	0.00789	0.00005	0.2398	0.0017	0.282904	0.000038	5.9	1.4	0.074
N26-47	0.282908	0.000043	1.467189	0.000030	0.00780	0.00009	0.2235	0.0027	0.282897	0.000043	5.6	1.5	0.074
N26-1	0.283033	0.000031	1.467153	0.000028	0.00639	0.00005	0.1788	0.0015	0.283024	0.000031	10.1	1.1	0.074
N26-14	0.282886	0.000040	1.467140	0.000035	0.00759	0.00019	0.2115	0.0052	0.282875	0.000040	4.9	1.4	0.074
N26-16	0.282879	0.000049	1.467160	0.000033	0.00675	0.00018	0.1847	0.0057	0.282869	0.000049	4.6	1.7	0.074
N26-17	0.282752	0.000042	1.467149	0.000037	0.00379	0.00010	0.1035	0.0033	0.282747	0.000042	0.3	1.5	0.074
N26-21c	0.282887	0.000034	1.467270	0.000036	0.00195	0.00005	0.0501	0.0015	0.282885	0.000034	5.2	1.2	0.074
N26-26	0.282981	0.000035	1.467188	0.000044	0.00552	0.00007	0.1574	0.0020	0.282973	0.000035	8.3	1.2	0.074
N26-13b	0.282861	0.000027	1.467232	0.000026	0.00209	0.00009	0.0517	0.0023	0.282858	0.000027	4.3	1.0	0.074
N26-11	0.282847	0.000028	1.467266	0.000034	0.00255	0.00006	0.0684	0.0022	0.282843	0.000028	3.7	1.0	0.074
N26-3b	0.282708	0.000038	1.467176	0.000038	0.00362	0.00008	0.0980	0.0023	0.282703	0.000038	-1.2	1.3	0.074
avearge											5.1		

These data suggest that the magma was primarily derived from a juvenile source, with a minor contribution from older crustal material. The older granodioritic dykes in the PO display higher initial εHf values, averaging +13.9 (Ismail et al., 2017), indicating that their felsic magmas evolved with little contamination from ancient continental crust. The contrasting Hf-isotope signature between the older granodioritic dyke and younger basaltic dyke can be attributed to i) increasing crustal recycling with time, ii) increasing crustal thickness, iii) contrasting tectonic setting or, more likely, a combination of all these (Zhuet al., 2021; Belousovaet al., 2010). The zircon εHf values of the PO basaltic dyke are similar to those of the gabbro in the Mawat ophiolite (Al Humadi et al., 2019) and

the gabbro in the Kermanshah ophiolite (Ao et al., 2016). Moreover, these mafic rocks also share a similar geochemical composition with the studied sample, showing alkaline and Mid-Ocean Rich Basalt (MORB) to back-arc basin (BAB) signature (Ao et al., 2016; Ismail et al., 2017; Al Humadi et al., 2019). In contrast, the older basalts, gabbros and norites of the PO show sub-alkaline compositions and a volcanic arc signature (Ismail et al., 2017).

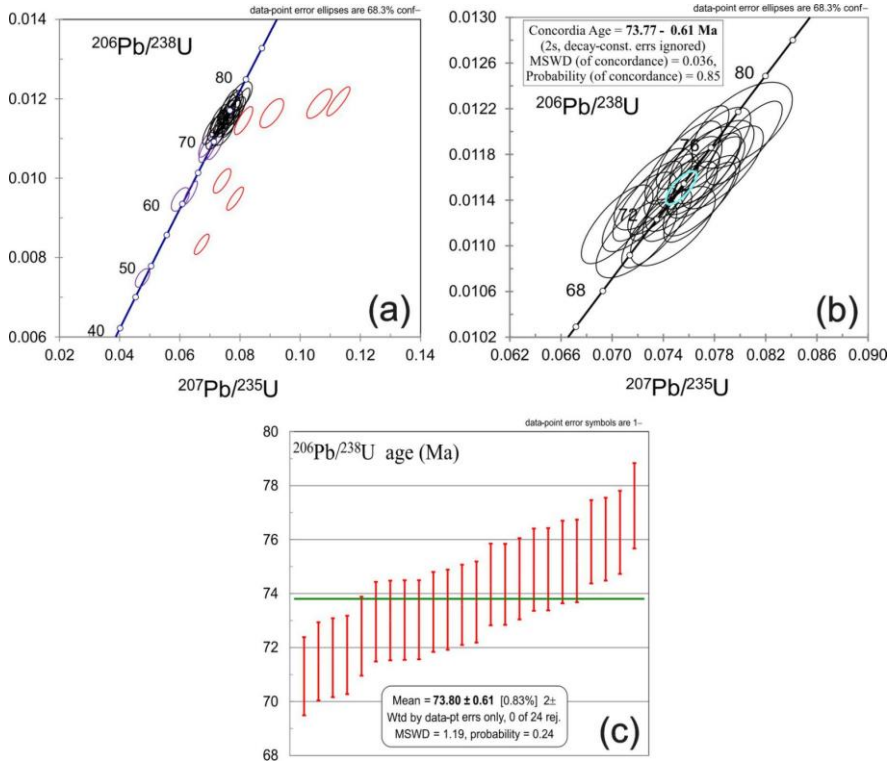

Fig. 6. U–Pb Concordia and $^{206}Pb/^{238}U$ weighted average diagrams of zircons from sample N26. a) Ages of zircons from basaltic sample N26 using a Nu AttoM single collector ICP-MS. The six analyses (purple colour) plot on a concordia curve showing a continuous decreasing range of $^{206}Pb/^{238}U$ ages from 70 to 48 Ma. The seven analyses (red colour) were omitted from the age calculations due to high discordancy. b) Concordia age of zircons from basaltic sample N26. c) Weighted average $^{206}Pb/^{238}U$ of zircons from sample N26

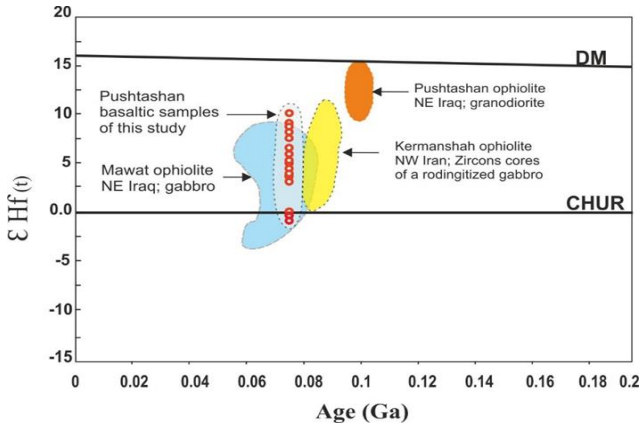

Fig. 7. εHf vs age diagram for the analyses from this study. Data from Pushtashan ophiolite (granodiorite), NE Iraq (Ismail et al., 2017), Mawat ophiolite (gabbro, Al Humadi et al., 2019) and Kermanshah ophiolite (rodingitized gabbro), NW Iran (Ao et al., 2016), are shown for comparison. CHUR = chondritic uniform reservoir (Bouvier et al., 2008); DM = Depleted Mantle (Griffin et al., 2000)

The magmatism along the ZOB was active from the Early Jurassic to Late Eocene ages (Monsef et al., 2018) and, in particular, the Late Cretaceous-Cenozoic magmatic rocks are widespread in the ZOB region. The magmatic event of the Late Cretaceous, bracketed between 95 Ma and 90 Ma is consistent with significant regional extension resulting from the initiation of subduction of the Neo-Tethyan ocean beneath the Iranian microcontinent (Kazemi et al., 2019). We suggest that the older arc-type basalts, gabbros and norites of the PO (Ismail et al., 2017) are also related to this event. Younger magmatic rocks are found within Neo-Tethyan ophiolites, and rocks after 90 Ma are interpreted to post-date the ophiolite emplacement. These include the 81 Ma MORB-type gabbro within the Mawat ophiolite about 70 km southeast of the PO, which is suggested to have developed in an extensional regime above a suprasubduction environment (Al Humadi et al., 2019).

Ali (2017) reported the 39 Ma gabbro from the Bulfat (aka Sardasht) ophiolite, which likewise shows MORB-type signature and is suggested to reflect arc rifting. Recently, a trondhjemite intrusion and plagiogranite from the Bulfat ophiolite were dated to 63.7 Ma and 50.6 Ma, respectively (Mohammad et al., 2023; Ao et al., 2020). Of these, the trondhjemite is suggested to have formed within an extensional regime in arc or back-arc related environment (Mohammad et al., 2023). Additionally, the Penjwen ophiolite has a 46 Ma trondhjemite (Ismail et al., 2020). There are two distinct ages of gabbros in the Kermanshah ophiolite, NW Iran. The older one (Harisn) is 79.3 Ma, while the younger one (Sahneh-Kamyaran) is 35.7 Ma in age (Ao et al., 2016). These both show MORB-like signature and are attributed to reflect continental rifting (Ao et al., 2016). The Kamyaran region and its western part (Taa-Baysaran) with the Oskul magmatic rocks in the Songor-Benah plutonic belt, are parts of a dismembered suprasubduction zone ophiolite of Miocene or later ages (Azizi et al. 2011). A gabbro and basalt from the Kamyaran region yield ages of 36.75 Ma and 54.6 Ma, respectively, which, in contrast, were formed in an island arc environment (Azizi et al. 2011).

The N-MORB-type basalts from the Oskul area have an age of 36.36 Ma and show characteristics of a back-arc basin environment (Azizi et al., 2011). Additionally, several igneous rocks with ages of ~ 40 Ma have been identified in the ZOB region. Granite and granodiorite rocks dated between 40 Ma and 39 Ma were documented within the uppermost section of the Sanandaj-Sirjan zone (Zhang et al., 2018). Cenozoic magmatism of ~ 50 Ma age is also prevalent in the northeastern ZOB (Dilek et al., 2010). In all, the zircon U-Pb ages indicate several magmatic episodes at 95-90 Ma, 81-74 Ma, 63-50 Ma, and 46-36 Ma, which reflect emplacement to post-emplacement magmatism related to the ZOB ophiolites. Moreover, each magmatic pulse has distinct geochemical signatures corresponding to the current tectonic environment. The above-mentioned ophiolites and localities are shown in Fig. 2, and the age data are compiled in Fig. 8.

5.2. Tectonic Framework

The collision of continental plates and their convergence play a significant role in the extensive magmatism found along the Alpine-Himalayan Orogenic Belt. This region is marked by magmatic rocks reflecting the events that evolved from the initiation of the subduction to the collision of the Neo-Tethyan Ocean, particularly along the ZOB. Dating the magmatic rocks linked to extensional and contractional episodes improves our understanding of the temporal framework of tectonic evolution of the ZOB during the Neo-Tethyan ocean subduction (Ismail et al., 2017; Ali et al., 2017; Ao et al., 2016, 2020; Al Humadi et al., 2019; Mohammad et al., 2023). The primary magmatic events of the Late Cretaceous ages of 95 Ma to 90 Ma mark the initiation of the subduction of the Neo-Tethyan Ocean beneath the Eurasian plate (Ali et al. 2012; Ismail et al. 2017; Al Humadi et al. 2019; Moghadam et al. 2021). This period is characterized by ongoing subduction influenced by an extensional or transtensional regime within a suprasubduction zone setting environment (Stern, 2004). Arc-related magmatism and supra-subduction zone ophiolite formation are the dominant features of

this stage (Omrani et al., 2008; Ali et al., 2012); this association likely indicates an extensional regime during the initiation of subduction (Agard et al., 2018).

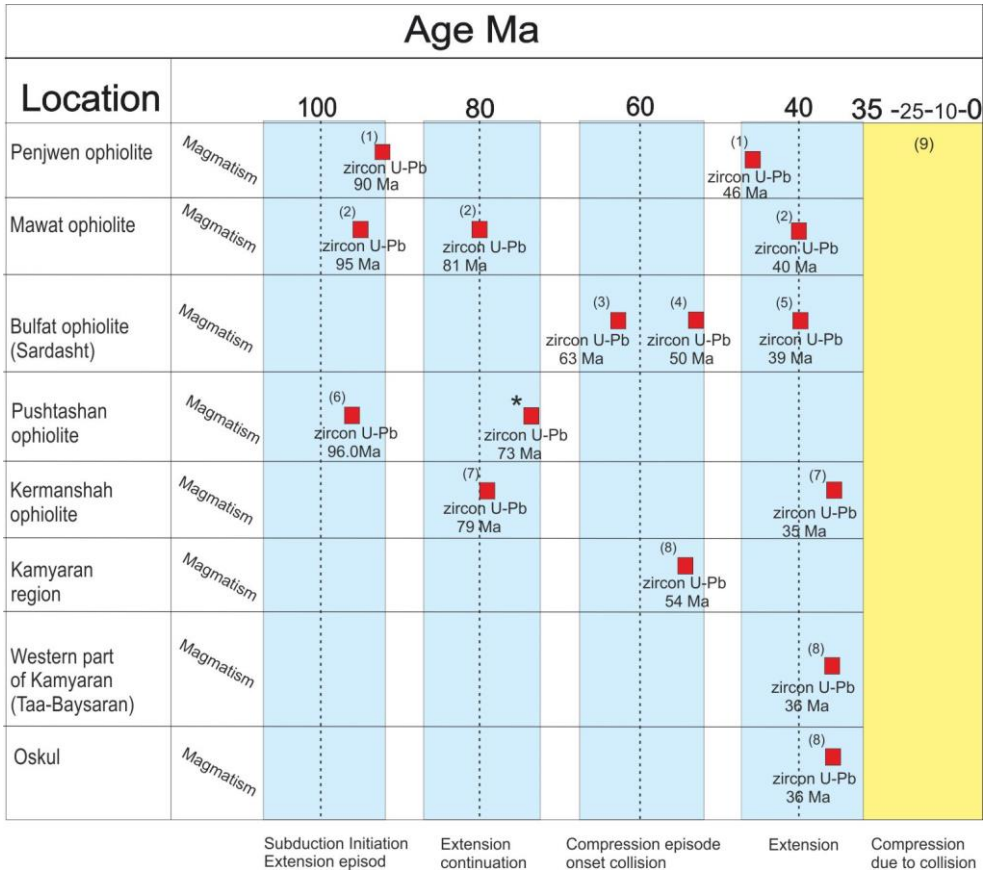

Fig. 8. Diagram illustrating the timing of the magmatic events in the ZOB. (1) (Ismailet al. 2020), (2) (Al Humadi et al. 2019), (3) (Mohammad et al., 2023), (4) (Ao et al., 2020), (5) (Ali, 2017), (6) (Ismail et al., 2017), (This study). (7) (Ao et al., 2016). (8) (Azizi et al., 2011). (9) The closure of the Neo-Tethys and the Arabia–Eurasia collision at ~35 Ma (Agard et al., 2005 and 2007). Crustal shortening and development of the Zagros fold-thrust belt occurred through the ages of 25-10 Ma (Mouthereau et al., 2012). During the ages of 10- 0 Ma, the Zagros evolved into a mature collisional zone (Allen et al., 2004)

The 74Ma basaltic dyke of this study, together with extensional magmatic events associated with the 81 Ma Mawat (Al Humadi et al., 2019) and 79Ma Kermanshah (Ao et al., 2016) ophiolites, likely reflects the continued rollback of the Neo-Tethyan slab. This tectonic process may have facilitated the back-arc extension and the formation of mafic to intermediate volcanic rocks (Agard et al., 2005). This is interpreted as a continuation of back-arc spreading or crustal thinning (Ali et al., 2019). The tectonic events occurring between 63.7Ma and 54.6 Ma are characterized by crustal thickening and arc-related subduction (Mouthereau et al., 2012). This period corresponds to the initial collision between the Arabian and Eurasian plates (Mohammad et al., 2014) and is characterized by the development of thrust fault systems and the deformation of ophiolites (Agard et al., 2011).

Thus, this period records the transition from extensional to contractional tectonic regime (Agard et al., 2005). It was followed by extensional episodes in the overriding plate leading to crustal thinning (Moghadam et al., 2020) and younger magmatic activity between 46Ma and 36Ma. The extension was likely triggered by slab break-off (Omrani et al., 2008. The following magmatic events are linked to the collision and overthrusting of the Arabian and Eurasian continents at 37Ma ($^{40}Ar/^{39}Ar$ muscovite, Mohammad et al., 2014). This crustal shortening partially overlaps with slab break-off-related

extensional magmatism and highlights the complex interplay of contraction and extension during the early collision.

5.3. Tectonic Switching Model

In general, E-MORB-type magmatism can be attributed to an extensional tectonic regime, whereas arc-type magmatism can be related to either extension or contraction (e.g., Xia and Li, 2019). However, the episodic nature of the magmatism could be linked to the changing tectonic regime, i.e., changes between crustal shortening (contraction) and crustal thinning (extension) (e.g., Wei et al., 2023). Therefore, to understand the magmatic evolution along the ZOB and at convergent plate margins in general, it is crucial to analyse the movement of the overriding plate relative to the subducting plate. This movement further leads to advancing and retreating subduction systems, each exhibiting distinct plate kinematics and magmatic features (Collins, 2002a; Cawood et al., 2009). This tectonic model, referred to as tectonic switching, explains the alternating pattern of long periods of extension followed by shorter (~10 Ma) episodes of contraction.

This cycle is driven by the retreat and advance of the subduction hinge, a process influenced by the arrival of buoyant oceanic plateaus at the trench (Collins, 2002a, 2002b). This model has been used to describe the evolution of both modern (e.g., Hermansson et al., 2008) accretionary orogens. Following the model and interpretation by Moghadam and Stern (2011) that many extensional events were associated with the Late Cretaceous subduction initiation and then reactivated by slab roll-back during the Eocene, we suggest the tectonic switching model best explains the tectonic evolution of the ZOB from the Late Cretaceous to Cenozoic. This model would explain that the subduction polarity of the Neo-Tethyan ocean continues to move N-NE beneath the Iranian microcontinent, as well as the magmatic flare-ups and time-related changes in the tectono-magmatic setting. We suggest that the high magmatic fluxes during the Late Cretaceous (95-74 Ma) and Eocene (45-35 Ma) represent an extensional episode, and that the magmatism interval during the Early Paleogene to Early Eocene (63-54 Ma) represents a contractional episode(s). Moreover, magmatism of the Late Cretaceous to Eocene ages in the ZOB in Iran is linked to the opening of a back-arc basin during an extension environment (Alavi, 1994).

Between ~ 35 Ma and 25 Ma, the tectonic settings in the ZOB shifted to a contractional regime, marking the Arabian and Eurasian plates collision (Allen et al., 2004; Agard et al., 2005; Omrani et al., 2008).

6. Conclusions

A younger magmatic event (basaltic dyke) is identified in the Pushtashan ophiolite, part of the Neo-Tethyan Ocean crust. The U-Pb zircon dating yields an age of 74 ± 1 Ma. The average initial ε_{Hf} value at 74 Ma is +5.1. The Hf isotope compositions of the parental magma during zircon crystallization suggest that it originated from a predominantly juvenile source, with minor contribution from an older crust. Based on our findings and comparison with other published chronological data, we suggest that the major magmatic events within the Zagros Orogenic Belt are closely linked to extensional and compression episodes that occurred during the subduction of the Neo-Tethyan Ocean. Four distinct magmatic age groups are identified: ~95–90 Ma, 81–74 Ma, 63–54 Ma, and 46–36 Ma. These are most likely associated with alternating phases of advancing and retreating subduction, suggesting the occurrence of tectonic switching processes within the Neo-Tethyan subduction system. This provides a coherent framework for understanding the magmatic and tectonic evolution of the Zagros Orogenic Belt from the Late Cretaceous to the Cenozoic

Acknowledgements

Arto Peltola is thanked for making the zircon mounts and the polished thin section. This is a Finnish Geosciences Research Laboratory contribution.

References

Agard, P., Jolivet, L., Vrielynck, B., Burov, E., Monié, P., 2018. Plate interface rheology and tectonic switching: Backarc vs. frontal subduction. Tectonophysics, 746, 572–589. https://doi.org/10.1016/j.lithos.2018.09.029

Agard, P., Omrani, J., Jolivet, L., Mouthereau, F., 2005. Convergence history across Zagros (Iran): constraints from collisional and earlier deformation. International Journal of Earth Science 94, 401e419. https://doi.10.1007/s00531-005-0481-4

Agard, P., Omrani, J., Jolivet, L., Whitechurch, H., Vrielynck, B., Spakman, W., Monié, P., Meyer, B., Wortel, R., 2011. Zagros orogeny: a subduction-dominated process. Geological Magazine. 148, 692-725. https://doi.10.1017/S001675681100046X

Al Humadi, H., Väisänen, M., Ismail, S.A., Kara, J., O'Brien, H., Lahaye, Y., Lehtonen, M., 2019. U-Pb geochronology and Hf isotope data from the Late Cretaceous Mawat ophiolite, NE Iraq. Heliyon, 5; e02721. https://doi.org/10.1016/j.heliyon.2019.e02721

Alavi, M., 1994. Tectonics of the Zagros orogenic belt of Iran: new data and interpretations. Tectonophysics, 229, 211–238. https://doi.org/10.1016/0040-1951(94)90030-2

Ali, S.A., 2017. 39 Ma U-Pb zircon age for the Shaki-Rash gabbro in the Bulfat igneous complex, Kurdistan region, Iraqi Zagros Suture Zone: rifting of an Intra-Neotethys Cenozoic arc. Ofioliti, 42, 69-80. https://doi.org/10.4454/ofioliti.v42i2.449

Ali, S.A., Nutman, A.P., Aswad, K.J., Jones, B.G., 2019. Overview of the tectonic evolution of the Iraqi Zagros thrust Zone: Sixty million years of Neotethyan ocean subduction. Journal of Geodynamics, 129, 162-177. https://doi.org/10.1016/j.jog.2019.03.007

Ali, S.A., Buckman, S., Aswad, K.J., Jones, B.G., Ismail, S.A., Nutman, A.P., 2012. Recognition of Late Cretaceous Hasanbag ophiolite-arc rocks in the Kurdistan Region of the Iraqi Zagros Suture Zone: A missing link in the palaeogeography of the closing Neotethys Ocean. Lithosphere, 4, 395-410.https://doi.org/10.1130/L207.1

Allen, M., Jackson, J., Walker, R., 2004. Late Cenozoic reorganization of the Arabia-Eurasia collision and the comparison of short-term and long-term deformation rates. Tectonics, 23(2). https://doi.org/10.1029/2003TC001530

Ao, S., Mao, Q., Khalatbari-Jafari, M., Windley, B.F., Song, D., Zhang, Z., Zhang, J., Wan, B., Han, C., Xiao, W., 2020. U–Pb age, Hf–O isotopes, and geochemistry of the Sardasht ophiolite in the NW Zagros orogen: Implications for the tectonic evolution of Neo-Tethys. Geological Journal, 563, 1315-1329. https://doi.org/10.1002/gj.4011

Ao, S., Xiao, W., Jafari, M.K., Talebian, M., Chen, L., Wan, B., Ji, W., Zhang, Z., 2016. U–Pb zircon ages, field geology and geochemistry of the Kermanshah ophiolite (Iran): from continental rifting at 79 Ma to oceanic core complex at ca. 36 Ma in the southern Neo-Tethys. Gondwana Research, 31, 305–318. https://doi.org/10.1016/j.gr.2015.01.014

Arai, S., Shimizu, Y., Ismail, S.A., Ahmed, A.H., 2006. Low-T formation of high-Cr spinel with apparently primary chemical characteristics within podiform chromitite from Rayat, northeastern Iraq. Mineralogical Magazine, 70, 499–508. https://doi.org/10.1180/0026461067050353

Aswad, K.J., Ali, S.A., Sheraefy, R.M.A., Nutman, A.P., Buckman, S., Jones, B.G., Jourdan, F., 2016. $^{40}Ar/^{39}Ar$ hornblende and biotite geochronology of the Bulfat igneous complex, Zagros Suture Zone, NE Iraq: new insights on complexities of Paleogene arc magmatism during closure of the Neotethys Ocean. Lithos 266, 406–413. https://doi.org/10.1016/j.lithos.2016.10.013

Azizi, H., Tanaka, T., Asahara, Y., Chung, S. L., Zarrinkoub, M.H., 2011. Discrimination of the age and tectonic setting for magmatic rocks along the Zagros Thrust Zone, northwest Iran, using the zircon U–Pb age and Sr–Nd isotopes. Journal of Geodynamics, 52, 304-320. https://doi.org/10.1016/j.jog.2011.03.001

Belousova, E. A., Griffin, W.L., O'Reilly, S.Y., 2006. Zircon crystal morphology, trace element signatures and Hf isotope composition as a tool for petrogenetic modelling: examples from Eastern Australian granitoids. Journal of Petrology, 47, 329-353. https://doi.org/10.1093/petrology/egi077

Belousova, E.A., Kostitsyn, Y.A., Griffin, W.L., Begg, G.C., O'Reilly, S.Y., Pearson, N.J., 2010. The growth of the continental crust: constraints from zircon Hf-isotope data. Lithos, 119, 457-466. https://doi.org/10.1016/j.lithos.2010.07.024

Bouvier, A., Vervoort, J.D., Patchett, P.J., 2008. The Lu–Hf and Sm–Nd isotopic composition of CHUR: Constraints from unequilibrated chondrites and implications for the bulk composition of terrestrial planets. Earth and Planetary Science Letters, 273, 48–57. https://doi.org/10.1016/j.epsl.2008.06.010

Buday T., Jassim S.Z., 1987. Tectonism, magmatism and metamorphism. The regional geology of Iraq, Iraq Geological Survey. GEOSURV. 2.

Cawood, P.A., Kröner, A., Collins, W.J., Kusky, T.M., Mooney, W.D., Windley, B.F., 2009. Accretionary orogens through Earth history. Geological Society, London, Special Publications, 318, 1–36. https://doi.org/10.1144/SP318.1

Coleman, R.G., 1977. Ophiolites, Ancient Oceanic Lithosphere. Springer-Verlag, Berlin, Heidelberg, New York.

Collins, W.J., 2002a. Hot orogens, tectonic switching, and creation of continental crust. Geology 30, 535–538. https://doi.org/10.1130/0091-7613(2002)030%3C0535:HOTSAC%3E2.0.CO;2

Dilek, Y., Imamverdiyev, N., Altunkaynak, S., 2010. Geochemistry and tectonics of Cenozoic volcanism in the Lesser Caucasus (Azerbaijan) and the peri-Arabian region: collision-induced mantle dynamics and its magmatic fingerprint. International Geology Review, 52(4-6), 536–578. https://doi.org/10.1080/00206810903360422

Dilek, Y.D., Robinson, P.T., 2003. Ophiolites in Earth history: introduction. Geological Society Special Publication, 218, 1-8. https://doi.org/10.1144/GSL.SP.2003.218.01.01

Fouad, S.F.A., 2015. Tectonic map of Iraq, scale 1: 1000 000, 2012. Iraqi Bulletin of Geology and Mining, 11(1), 1–7.

Furnes, H., Dilek, Y., 2017. Geochemical characterization and petrogenesis of intermediate to silicic rocks in ophiolites: A global synthesis. Earth Science Reviews, 166, 1-37. https://doi.org/10.1016/j.earscirev.2017.01.001

Furnes, H., Dilek, Y., Zhao, G., Safonova, I., Santosh, M., 2020. Geochemical characterization of ophiolites in the Alpine-Himalayan Orogenic Belt: Magmatically and tectonically diverse evolution of the Mesozoic Neotethyan oceanic crust. Earth Science Reviews, 103258. https://doi.org/10.1016/j.earscirev.2020.103258

Gerdes, A., Zeh, A., 2006. Combined U-Pb and Hf isotope LA-MC-ICPMS analyses of detrital zircons: Comparison with SHRIMP and new constraints for the provenance and age of an Armorican metasediment in Central Germany. Earth and Planetary Science Letters, 249, 47-61. https://doi.org/10.1016/j.epsl.2006.06.039

Ghasemi, A., Talbot, C. J., 2006. A new tectonic scenario for the Sanandaj–Sirjan Zone (Iran). Journal of Asian Earth Sciences, 26(6), 683-693. https://doi.org/10.1016/j.jseaes.2005.01.003

Griffin, W.L., Pearson, N.J., Belousova, E., Jackson, S.V., Van Achterbergh, E., O'Reilly, S.Y., Shee, S.R., 2000. The Hf isotope composition of cratonic mantle: LAMMC-ICPMS analysis of zircon megacrysts in kimberlites. Geochimica et Cosmochimica Acta. 64, 133–147. https://doi.org/10.1016/S0016-7037(99)00343-9

Heinonen, A.P., Andersen, T., Rämö, O.T., 2010. Re-evaluation of rapakivi petrogenesis: Source constraints from the Hf isotope composition of zircon in the rapakivi granites and associated mafic rocks of Southern Finland. Journal of Petrology, 51, 1687-1709. https://doi.org/10.1093/petrology/egq035

Hermansson, T., Stephens, M. B., Corfu, F., Page, L.M., Andersson, J., 2008. Migratory tectonic switching, western Svecofennian orogen, central Sweden: Constraints from U/Pb zircon and titanite geochronology. Precambrian Research, 161(3-4), 250-278. https://doi.org/10.1016/j.precamres.2007.08.008

Huhma, H., Mänttäri, I., Peltonen, P., Kontinen, A., Halkoaho, T., Hanski, E., Hokkanen, T., Hölttäa, P., Juopperi, H., Konnunaho, J., Lahaye, Y., Luukkonen, E., Pietikäinen, K., Pulkkinen, A., Sorjonen-Ward,

P., Vaasjoki, M., Whitehouse, M., 2012. The age of the Archaean greenstone belts in Finland. Geological Survey of Finland Special Paper. 54, 74–175.

Ismail, S. A., Koshnaw, R. I., Barber, D. E., Al Humadi, H., Stockli, D. F., 2020. Generation and exhumation of granitoid intrusions in the Penjween ophiolite complex, NW Zagros of the Kurdistan region of Iraq: Implications for the geodynamic evolution of the Arabian-Eurasian collision zone. Lithos, 376, 105714. https://doi.org/10.1016/j.lithos.2020.105714

Ismail, S.A., Ali, S.A., Nutman, A.P., Bennett, V.C., Jones, B.G., 2017. The Pushtashan juvenile suprasubduction zone assemblage of Kurdistan NE Iraq: A Cretaceous (Cenomanian) Neo-Tethys missing link. Geoscience Frontiers, 8, 1073–1087. https://doi.org/10.1016/j.gsf.2016.11.002

Jassim S.Z., Goff J.C., 2006. Geology of Iraq. Brno, Dolin, Prague and Moravian Museum, Czech Republic.

Kara, J., Väisänen, M., Johansson, A., Lahaye, Y., O'Brien, H., Eklund, O., 2018. 1.90–1.88 Ga arc magmatism of central Fennoscandia: geochemistry, U-Pb geochronology, Sm-Nd and Lu-Hf isotope systematics of plutonic-volcanic rocks from southern Finland. Geologica Acta 16, 1–23. https://doi.org/10.1344/GeologicaActa2018.16.1.1

Kazemi, Z., Ghasemi, H., Tilhac, R., Griffin, W., Moghadam, H.S., O'Reilly, S., Mousivand, F., 2019. Late Cretaceous subduction-related magmatism on the southern edge of Sabzevar basin, NE Iran. Journal of the Geological Society, 176, 530-552. https://doi.org/10.1144/jgs2018-076

Kemp, A.I.S., Foster, G.L., Schersten, A., Whitehouse, M.J., Darling, J., Storey, C., 2009a. Concurrent Pb-Hf isotope analysis of zircon by laser ablation multi-collector ICPMS, with implications for the crustal evolution of Greenland and the Himalayas. Chemical Geology, 261, 242-258. https://doi.org/10.1016/j.chemgeo.2008.06.019

Kemp, A.I.S., Hawkesworth, C.J., Collins, W.J., Gray, C.M., Blevin, P.L., EIMF, 2009b. Isotopic evidence for rapid continental growth in an extensional accretionary orogen: the Tasmanides, eastern Australia. Earth and Planetary Science Letters 284, 455–466. https://doi.org/10.1016/j.epsl.2009.05.011

Kinny, P.D., Maas, R., 2003. Lu–Hf and Sm–Nd isotope systems in zircon. Reviews in Mineralogy and Geochemistry, 53, 327–341. https://doi.org/10.2113/0530327

Kirkland, C.L., Smithies, R.H., Taylor, R.J.M., Evans, N., McDonald, B., 2015. Zircon Th/U ratios in magmatic environs. Lithos 212, 397–414. https://doi.org/10.1016/j.lithos.2014.11.021

Ludwig, K.R., 2003. User's manual for isoplot/ex, version 3.00. A geochronological toolkit for Microsoft Excel. Berkeley Geochronology Centre Special Publication, 4, 25–32.

Moghadam, H.S., Stern, R.J., Griffin, W.L., Khedr, M.Z., Kirchenbaur, M., Ottley, C.J., Whattam, S.A., Kimura, J.I., Ghorbani, G., Gain, S., O'Reilly, S.Y., Tamura, A., 2020. Subduction initiation and back-arc opening north of Neo-Tethys: Evidence from the Late Cretaceous Torbat-e-Heydarieh ophiolite of NE Iran. Geological Society of America Bulletin, 132, 1083-1105. https://doi.org/10.1130/b35065.1

Moghadam, H.S., Stern, R.J., 2011. Geodynamic evolution of Upper Cretaceous Zagros ophiolites: formation of oceanic lithosphere above a nascent subduction zone. Geological Magazine, 148, 762–801. https://doi.org/10.1017/S0016756811000410

Mohammad, Y.O., Abdulla, K., Azizi, H., 2023. Late Cretaceous-Paleocene Arc and Back-Arc System in the Neotethys Ocean, Zagros Suture Zone. Minerals, 13, 1367. https://doi.org/10.3390/min13111367

Mohammad, Y.O., Cornell, D.H., 2017. U–Pb zircon geochronology of the Daraban leucogranite, Mawat ophiolite, Northeastern Iraq: a record of the subduction to collision history for the Arabia–Eurasia plates. Island Arc 26, e12188. https://doi.org/10.1111/iar.12188

Mohammad, Y.O., Cornell, D.H., Qaradaghi, J.H., Mohammad, F.O., 2014. Geochemistry and Ar-Ar muscovite ages of the daraban leucogranite, Mawat ophiolite, northeastern Iraq: implications for Arabia–Eurasia continental collision. Journal of Asian Earth Sciences, 86, 151–165. https://doi.org/10.1016/j.jseaes.2013.09.029

Monsef, I., Monsef, R., Mata, J., Zhang, Z., Pirouz, M., Rezaeian, M., Ismaeili, R., Xiao, W., 2018. Evidence for an early-MORB to fore-arc evolution within the Zagros Suture Zone: Constraints from zircon U-Pb geochronology and geochemistry of the Neyriz ophiolite (South Iran). Gondwana Research, 62, 287-305. https://doi.org/10.1016/j.gr.2018.03.002

Morel, M.L.A., Nebel, O., Nebel-Jacobsen, Y.J., Miller, J.S., Vroon, P.Z., 2008. Hafnium isotope characterization of the GJ-1 zircon reference material by solution and laser-ablation MC-ICPMS. Chemical Geology, 255, 231 235. https://doi.org/10.1016/j.chemgeo.2008.06.040

Mouthereau, F., Lacombe, O., and Vergés, J., 2012. Building the Zagros collisional orogen: Timing, strain distribution, and the dynamics of Arabia/Eurasia plate convergence. Tectonophysics, 532–535, 27–60. https://doi.org/10.1016/j.tecto.2012.01.022

Müller, W., Shelley, M., Miller, P., Broude, S., 2009. Initial performance metrics of a new custom-designed ArF excimer LA-ICPMS system coupled to a two-volume laser-ablation cell. Journal of Analytical Atomic Spectrometry, 24, 209-214. https://doi.org/10.1039/B805995K

Omrani, J., Agard, P., Whitechurch, H., Benoit, M., Prouteau, G., Jolivet, L., 2008. Arc-magmatism and subduction history beneath the Zagros Mountains, Iran: A new report of adakites and geodynamic consequences. Lithos, 106, 380–398. https://doi.org/10.1016/j.lithos.2008.09.008

Patchett, P., Tatsumoto, M., 1981. Lu/Hf in chondrites and definition of a chondritic hafnium growth curve. Lunar Planetary Science, 12, 822–824. https://doi.org/10.1016/S0012-821X(97)00040-X

Pearce, J.A., 2014. Immobile element fingerprinting of ophiolites. Elements, 10, 101-108. https://doi.org/10.2113/gselements.10.2.101

Scherer, E.E., Münker, C., Mezger, K., 2001. Calibration of the lutetium hafnium clock. Science, 293, 683-687. https://doi.org/10.1126/science.1061372

Şengör, A.C., 1984. The Cimmeride orogenic system and the tectonics of Eurasia. https://doi.org/10.1130/SPE195-p1

Stern, R.J., 2004. Subduction initiation: spontaneous and induced. Earth and Planetary Science Letters, 226, 275-292. https://doi.org/10.1016/j.epsl.2004.08.007

Söderlund U, Patchett PJ, Vervoort J, Isachsen CE., 2004. The 176 Lu decay constant determined by Lu-Hf and U-Pb isotope systematics of Precambrian mafic intrusions. Earth and Planetary Science Letters, 219, 311-324. https://doi.org/10.1016/S0012-821X(04)00012-3

Van Achterbergh, E., Ryan, C., Jackson, S., Griffin, W., 2001. Appendix 3 Data reduction software for LA-ICP-MS. In: Sylvester, P. (Ed.), Laser-Ablation-ICPMS in the Earth Sciences, MAC., Short Course, 239-243.

Vervoort, J.D., Patchett, P.J., Soderlund, U., Baker, M., 2004. Isotopic composition of Yb and the determination of Lu concentrations and Lu/Hf ratios by isotope dilution using MC-ICPMS. Geochemistry, Geophysics Geosystems Journal, 5, Q11002. https://doi.org/10.1029/2004GC000721

Wei, W., Lin, W., Chen, Y., Faure, M., Ji, W., Hou, Q., Yan, Q., Wang, Q., 2023. Tectonic controls on magmatic tempo in an active continental margin: Insights from the Early Cretaceous syn-tectonic magmatism in the Changle-Nan'ao Belt, South China. Journal of Geophysical Research: Solid Earth, 128, e2022JB025973. https://doi.org/10.1029/2022JB025973

Xia, L., Li, X., 2019. Basalt geochemistry as a diagnostic indicator of tectonic setting. Gondwana Research, 65, 43-67. https://doi.org/10.1016/j.gr.2018.08.006

Zhang, Z., Xiao, W., Ji, W., Majidifard, M.R., Rezaeian, M., Talebian, M., Xiang, D., Chen, L., Wan, B., Ao, S., Esmaeili, R., 2018. Geochemistry, zircon U-Pb and Hf isotope for granitoids, NW Sanandaj-Sirjan zone, Iran: implications for Mesozoic-Cenozoic episodic magmatism during Neo-Tethyan lithospheric subduction. Gondwana Research, 62, 227–245. https://doi.org/10.1016/j.gr.2018.04.002

Zhu, Z., Ding, Y., Li, Z., Dong, Y., Wang, H., Liu, J., Zhu, J., Li, X., Chu, F., Jin, X., 2021. Hafnium isotopic constraints on crustal assimilation in response to the tectono–magmatic evolution of the Okinawa Trough. Lithos, 398, 106352. https://doi.org/10.1016/j.lithos.2021.106352